

# **Arginine-Specific Molecularly Imprinted Polymer-Based Laser-Induced Graphene Flexible Sensor**

Ruotong Gao¹, Muhammad Khatib¹, Kuang-Jung Hsu¹, and Zhenan Bao¹ <sup>™</sup>

<sup>1</sup>Department of Chemical Engineering, Stanford University, Stanford, CA 94305, USA.

Received: day month year; Revised: day month year; Accepted: day month year (automatically inserted by the publisher)

Address correspondence to Zhenan Bao, zbao@stanford.edu



Cite this article: Nano Research, xxxx, xx, 949xxxxx. https://doi.org/(automatically inserted by the publisher)

ABSTRACT: Non-invasive monitoring of biomarkers is crucial for the wide adoption of health monitoring and the early detection of health conditions. L-Arginine, a conditionally essential amino acid with a variety of significant physiological roles, is critical for the pathogenesis of various cardiovascular diseases (CVD) such as endothelial dysfunction, neurodegenerative disorders, and overall homeostasis. However, current methods of detection of L-Arginine are unsuitable for continuous monitoring due to their heavy requirements on resources and invasive sampling. Here, we describe the fabrication of an L-Arginine-specific electrochemical sensor by integrating a Molecularly Imprinted Polymer (MIP) on a PEDOT:PSS modified Laser-Induced Graphene (LIG) electrode on a flexible substrate. The MIPs function as sensitive and selective synthetic receptors for L-Arginine, while the PEDOT:PSS electrodeposited LIG electrode provides low impedance and a high sensitivity detection. The MIP-PEDOT:PSS-LIG platform uses Electrochemical Impedance Spectroscopy (EIS) and demonstrates exceptional analytical performance, achieving a low Limit of Detection (LOD) (~1 nm) and a wide linear dynamic range (1 nM to 1 mM), effectively covering the physiologically relevant concentrations of arginine in sweat. The sensor exhibited high selectivity against structurally similar amino acids (lysine, histidine, and citrulline) and maintained robust linearity (R2 ~ 0.98) when tested in an artificial sweat medium. Furthermore, the device exhibited excellent reusability and stability via controlled electrostatic regeneration, demonstrating robustness and applicability within artificial sweat. In summary, a sensitive and selective MIP is developed which enables non-invasive sensing of L-arginine with readily made flexible electrodes and provides a promising device for next-generation point-of-care diagnostics and health monitoring.

**KEYWORDS:** Molecularly Imprinted Polymer, L-Arginine, Flexible Sensors, Laser-Induced Graphene, Electrochemical Impedance Spectroscopy

# 1 Introduction

Developing real-time molecular sensors is important towards continuous health monitoring [1-5]. Traditional biomarker analysis relies heavily on blood sampling, which provides a comprehensive metabolic panel but requires invasive procedures, a heavy expenditure of manpower and time, and is therefore unsuitable for continuous use and monitoring [1, 5, 6]. This has spurred significant interest in analyzing alternative biofluids such as interstitial fluid, saliva, and sweat for non-invasive and minimally-invasive health monitoring. The development of sweat sensors has garnered significant attention within the recent literature [7–9]. Sweat contains a variety of important analytes such as electrolytes, metabolites, hormones, and proteins, all of which can aid in creating a comprehensive profile reflecting homeostasis and potential pathological conditions. [10, 11]. The appeal of sweat sensors lies in their non-invasive and wearable nature, suitable for continuous and real-time monitoring without the discomfort and risks present within traditional sampling methods [12]. Amino acids stand as pathologically and physiologically significant biomarkers that warrant interest in their potential for continuous and real-time monitoring [13–15]. Past research with amino acid liquid chromatography demonstrates a substantial concentration of amino acids within

sweat with demonstrated concentration-dependent correlations between both biofluids (though these connections still require further investigation) [16, 17]. Further analysis by Kuroki and Tsunado demonstrates intra- and inter-day stability in sweat amino acid concentrations regardless of sex [18]. This demonstrates the increasing feasibility in integrating wearables for amino acid detection in health monitoring. Among the various amino acids present in sweat, L-Arginine is of particular significance due to its various roles in health conditions, prevalence in sweat (97.01  $\pm$  67.42  $\mu M$ ), and sheer importance in physiological function [17, 19].

L-Arginine is an endogenous conditionally essential amino acid traditionally associated with the urea cycle through facilitating the detoxification of ammonia and aiding renal function [20]. Furthermore, L-Arginine also plays a significant role as a precursor for other critical molecules, including creatine (involved in energy metabolism), proline and collagen (wound healing and tissue repair), and polyamines (involved in cell growth), and plays a significant role in the immune response [19, 21, 22]. Its most studied and significant role is in the nitric oxide (NO) pathway, where it acts as the sole source of nitrogen for NO synthesis [23–26]. L-Arginine is the primary substrate in which the enzyme endothelial nitric oxide synthase (eNOS) produces NO in endothelial cells. Low NO levels are associated with

oxidative stress, further damaging the endothelium and promoting atherosclerosis by facilitating the oxidation of low-density lipoprotein (LDL) cholesterol and the subsequent inflammatory response within arterial walls [27]. The loss of endothelial NO is the central mechanism in the pathogenesis of endothelial dysfunction and vascular dysregulation [28, 29]. Defects in the Larginine: NO pathway have been linked to a variety of cardiovascular diseases (CVD) such as hypertension, atherosclerosis, coronary artery diseases (CAD), and peripheral artery disease (PAD), and more, as well as pathophysiology in several CNS complications such as acute brain injuries (e.g., stroke, traumatic brain injury) and chronic neurodegenerative diseases such as Alzheimer's disease. [23, 25, 28, 30, 31, 32]. L--Arginine, with its multifaceted physiological impact and predecessor relation to nitric oxide, is hence a promising diagnostic biomarker for CVD, CNS health, metabolic health, and immune status. Traditional methods of sweat detection of Larginine rely on analytical techniques such as High-Performance Liquid Chromatography (HPLC) and Liquid Chromatography Mass Spectrometry (LC-MS/MS) [17, 18]. These methods offer high sensitivity and precision in various biological matrices but have high operational costs, time-consuming protocols, and the need for specialized expertise, therefore rendering them unsuitable for point-of-care or continuous monitoring applications. L-Arginine sensors have been previously produced using mostly enzymic and optical methods, with instances of enzymic amperometric sensors for arginine detection through the enzyme arginine deiminase [33, 34]; enzymic potentiometric sensors, commonly using the enzymes urease and arginase [35, 36]; and optical ratiometric sensors, such as through optical of arginine-induced disintegration supramolecular assembly [37]. Many of these enzymatic sensors, however, lack selectivity and can offer false positives through the detection of other amino acids [38, 39]. Current literature has yet to demonstrate the detection of L-Arginine in a flexible device, especially with high sensitivity, selectivity, robustness, and reversibility.

Molecularly imprinted polymers (MIPs), or synthetic antibodies, have shown considerable potential for highly sensitive and selective detection as a sensing agent for usage within a biological medium [40, 41]. MIPs are synthetic polymers that are engineered to create specific molecular binding sites within polymeric matrices for the target molecule through a template-assisted polymerization synthesis with crosslinked monomers in the presence of the target analyte molecules, leaving behind complementary cavities that can bind target compounds with high specificity, akin to natural receptors or antibodies [42]. This technology offers several advantages, including selectivity, scalability, stability, and reusability, making MIPs particularly suitable for detecting endogenous metabolites [40, 43]. The integration of such sensors into wearable platforms necessitates materials that are not only highly sensitive but also flexible and robust [3, 8]. Laser-induced graphene (LIG) has emerged as a promising material for this purpose due to its facile and costeffective fabrication via direct laser writing on polymer substrates, offering a scalable approach for creating intricate electrode patterns [44]. LIG electrodes possess a unique porous 3D structure, providing a high surface area and excellent electrical conductivity, which significantly enhances the sensitivity and performance of electrochemical biosensors [45, 46]. Furthermore, its inherent flexibility and ready integration with flexible and skin-like substrates allows for further compatibility with the skin and access to biofluids, enhancing biocompatibility [46, 47]. Furthermore, we found in this work that the integration of electroconductive polymers like PEDOT:PSS can serve to further improve the LOD of a device and mitigate some of the inherent inter- electrode variability across LIG samples. In this study, we developed an L-Arginine-specific MIP integrated in a PEDOT:PSS electrodeposited laser-induced graphene electrode to create a flexible, sensitive, selective, and reusable electrochemical sensor. The MIP sensor functions via the analyte's binding with the recognition cavities which impedes ion transport to the electrode surfaces, subsequently increasing the impedance of the entire system (detected/monitored through EIS), which rises with analyte concentration until the MIP is saturated. By combining the selectivity of MIPs with flexible electronics, our sensor demonstrates the highly sensitive, noninvasive sensing of L-arginine, offering a promising and viable approach for the early detection/management of numerous health conditions and furthering development of next-generation wearable molecular sensors.

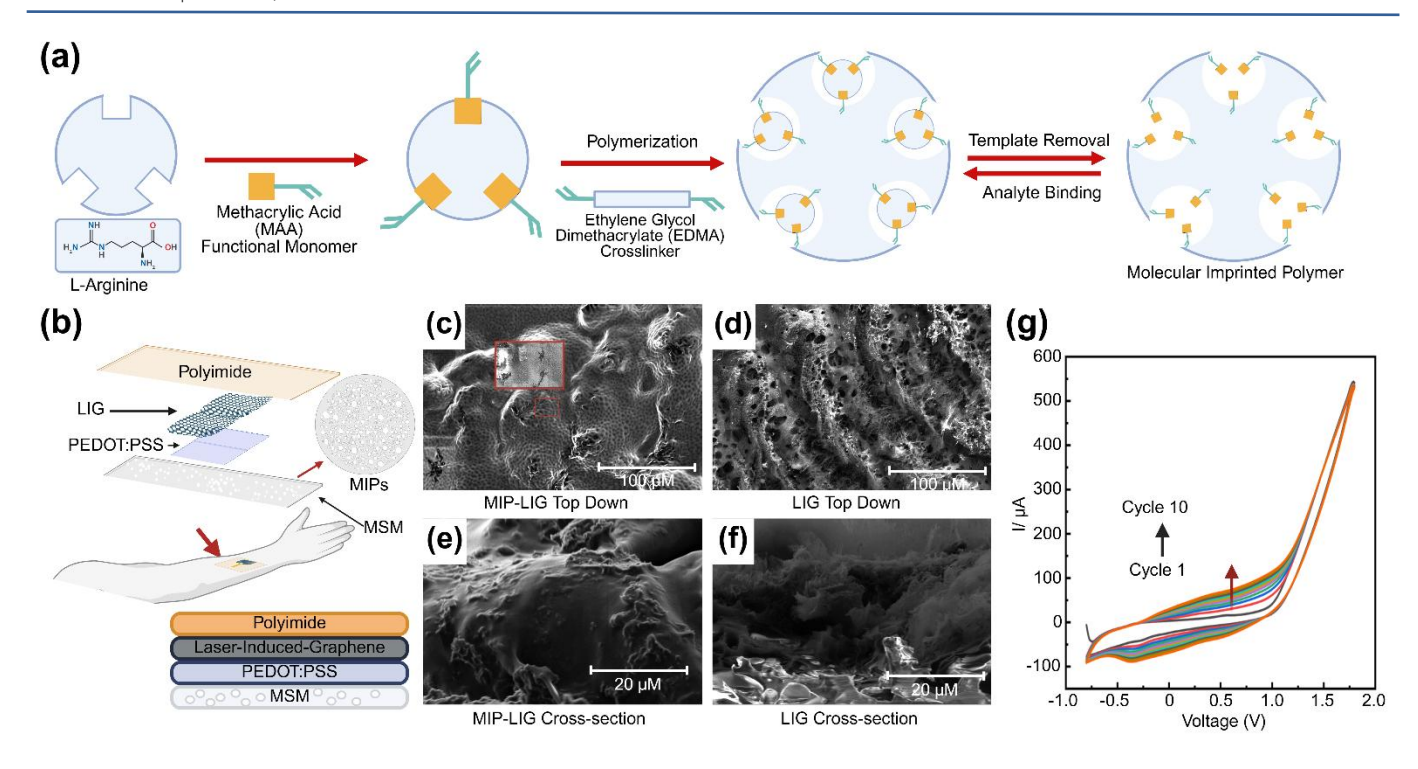


Figure 1. Schematic and Microscopic Images of the Arginine-Specific MIP Sensor. (a) The synthesis process for the L-arginine molecularly imprinted polymer (MIP). The template molecule (L-Arginine) and functional monomer (Methacrylic Acid, MAA) form a complex, which is then polymerized with a cross-linker (Ethylene Glycol Dimethacrylate, EDMA). Subsequent removal of the template leaves recognition cavities for selective analyte binding. (b) Illustration of the flexible sensor device designed for non-invasive sweat analysis on the forearm. (c) Top-down SEM image showing the sensor electrode tip (MIP-LIG) after cutting (red circled regions: visible nanoparticles from MIP). (d) A top-down SEM image displaying LIG morphology as a control (e) SEM image showing the cross-section of the sensor electrode tip after cutting (visible nanoparticle formation). (f) SEM image showing the cross-section of the LIG tip (No MIP or PEDOT) after cutting. (g) PEDOT:PSS electrodeposition cyclic voltammetry (CV) cycles (10) -0.8 to 1.8V at 50 mV/s

# 2 Results and Discussion

# 2.1 Sensor Creation

The key in developing the selective sensing interface is the successful synthesis of a molecularly imprinted polymer (MIP) tailored for L-Arginine recognition. The synthesis process (Fig. 1a) employs molecular imprinting through free-radical bulk polymerization to generate selective recognition sites. L-Arginine first forms a pre-polymerization complex with Methacrylic Acid (MAA), the functional monomer, which is subsequently crosslinked using Ethylene Glycol Dimethacrylate (EDMA). This MIP is then mixed with a polymer binder (poly(vinyl chloride) (PVC)) and dip coated as a thin film to create a molecular selective membrane (MSM) integrated into a flexible, multilayered device designed for continuous, noninvasive sweat analysis on the skin (Fig. 1b). The top-down view SEM images (Fig. 1c (MIP-PEDOT/LIG) and 1d (LIG-only)) show a clear difference in morphology after MIP and PEDOT deposition. Cross-sectional images of the MIP-modified electrode tip (Fig. 1e-f) further confirmed successful MIP adhesion, characterized

by the presence of distinct nanoparticles and integration. In contrast, the bare Laser-Induced Graphene (LIG) sensor tip (Fig. 1f) exhibited a feathery and less dense structure, confirming the morphological changes induced by the MIP layer. The PEDOT:PSS electrodeposition was conducted through cyclic voltammetry (CV), and cycles recorded during this process (Fig. 1g) show the steady growth of current over successive cycles as well as visible morphological changes, confirming successful deposition. This was further confirmed by the SEM top-view (Fig. S1 in the Electronic Supplementary Information (ESM)) and cross-sectional view (Fig. S1 in the ESM) as indicated by the fibrous morphology from PEDOT:PSS. We found that ten cycles of CV demonstrated the optimal, and most efficient, impedance result for the PEDOT:PSS electrodeposition (Fig. S2 in the ESM). Furthermore, Raman Spectroscopy was conducted to further characterize the laser-induced graphene electrode we used within the sensor, with characteristic peaks of graphitic materials (D peak at ~1350 cm<sup>-1</sup>, G peak at ~1580 cm<sup>-1</sup>, 2D peak at ~2700 cm<sup>-1</sup>), confirming the successful formation of laser-induced defective and multi-layered graphene (Fig. S3 in the ESM). These characterization results confirm the successful creation of MIPadhered PEDOT:PSS-LIG electrodes.

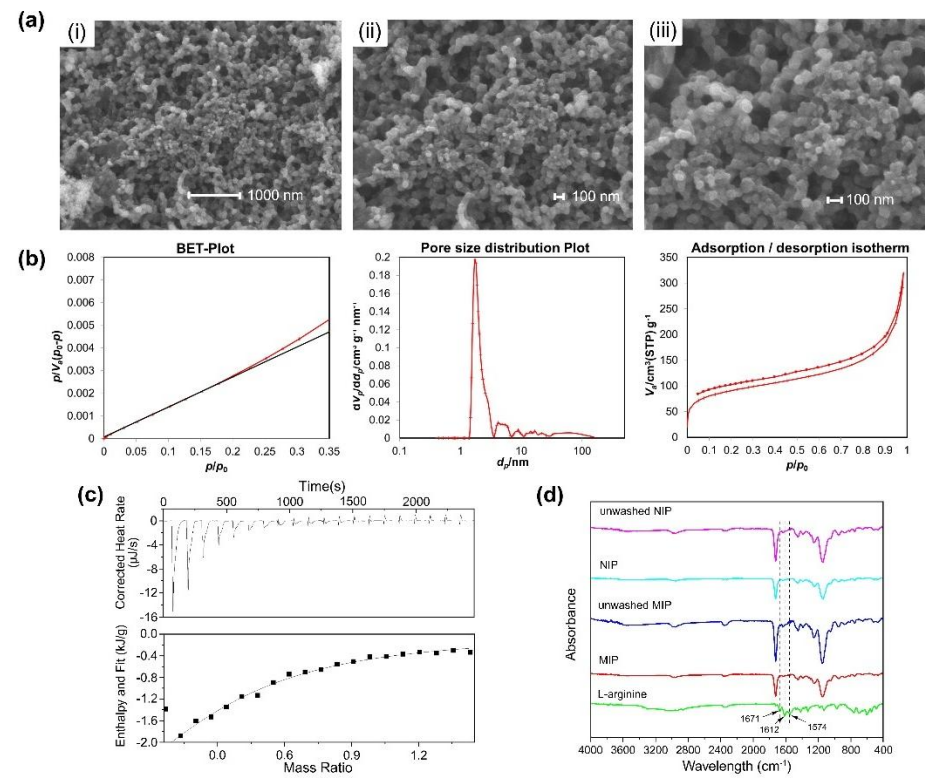


Figure 2. (a) High-resolution SEM images of the synthesized MIP particles, revealing an irregular, porous morphology composed of aggregated nanospheres (i) 20kX Zoom, (ii) 30kX Zoom, (iii) 50kX Zoom of MIPs. (b) Brunauer–Emmett–Teller (BET) and Barrett–Joyner–Halenda (BJH) analysis results. The plots confirm a significant difference in surface area between the MIP (301.6 m2/g) and NIP (128.2 m²/g) and a mesoporous structure with an average pore diameter of 4.68 nm for the MIP. (c) Isothermal Titration Calorimetry (ITC) Time to Corrected Heat Ratio (up) and Mass Ratio to Enthalpy and Fit data (down) for the MIP-arginine binding interaction. The exothermic enthalpy of (-3.86 kJ/mol-1) indicates successful and favorable binding within the imprinted cavities. (d) Fourier-Transform Infrared Spectroscopy (FT-IR) spectra comparing unwashed and washed MIPs and NIPs with the L-arginine template. The disappearance of characteristic arginine peaks (e.g., at 1671 cm-1) in the washed MIP confirms the complete removal of the template molecule [48].

# 2.2 MIP Characterization and Morphology

The SEM images revealed that both the MIP and Non-Imprinted Polymer (NIP, made without L-Arginine templates) consist of irregularly shaped agglomerates of nanospheres (Fig. 2a, Fig S4). A notable qualitative difference was observed in the surface topography, where the MIP surface presented a discernibly rougher and more porous morphology as compared to the smoother surface of the NIP (Fig. S5 in the ESM). Furthermore, we used Brunauer-Emmett-Teller (BET) and Barrett-Joyner-Halenda (BJH) analyses to quantitatively characterize the specific surface area and porosity of the polymers. The specific surface area for the MIP was measured as 301.6 m<sup>2</sup>/g (Fig. 2b), compared to the 128.2 m<sup>2</sup>/g measured for the NIP (Fig. S5 a, b in the ESM). This indicates a significant difference in porosity, with BJH adsorption-desorption analysis further determining the porous nature of the materials and confirming a mesoporous structure for the MIP. The pore volume of the MIP (0.558 cm<sup>3</sup>/g) was substantially larger than that of the NIP (0.334 cm<sup>3</sup>/g), an average nanoparticle size of 19.8961 nm, and an average MIP pore diameter of 4.68 nm. Spectroscopic and thermodynamic characterizations were subsequently performed to validate the chemical integrity and binding functionality of the polymers. The thermodynamics of the binding interaction were quantified using Isothermal Titration Calorimetry (ITC). The analysis of the MIP-L-Arginine interaction yielded a negative enthalpy change (ΔH) of -4.76 kJ/mol, indicating a spontaneous and enthalpically favorable exothermic binding event, though it is in the lower binding energies of conventional MIPs. Such a reaction is characteristic of the formation of favorable non-covalent interactions, such as hydrogen bonding and Van der Waals interactions, between the analyte and the functional monomers

within the pre-organized cavity. In contrast, the ITC data for the NIP revealed no significant change in enthalpy with a  $(\Delta H)$  of -1.61 kJ/mol, out of the range for meaningful binding energy, confirming a lack of recognizable thermodynamic binding (Fig S5 c-d) [49]. However, it is important to note that the MIP's binding affinity stands on the lower end of binding affinities observed in the current literature [49]. This low binding affinity was attributed to the addition of trifluoroacetic acid (TFA) to enhance solubility during the synthesis [42]. L-Arginine is inherently a highly polar molecule and is among the most polar of all amino acids, making it exceptionally challenging to identify an ideal solvent for MIP polymerization so that all components are soluble. We found that polar aprotic solvents such as dichloromethane and tetrahydrofuran can only dissolve limited amount of L-Arginine due to its high polarity. Addition of TFA was conducted in accordance with previous reports on creating Phenylalanine-detecting MIPs [48, 49]. This lower binding affinity still resulted in good sensitivity and selectivity of the resulting MIPs for detection purposes, demonstrated later by the clear EIS trends, low LOD, and large linear range of L-Arginine EIS detection. Overall, the ITC results demonstrate that the preorganized cavities do create preferential binding in the MIP. Additionally, Fourier-Transform Infrared Spectroscopy (FT-IR) provided spectroscopic evidence of complete template removal (Fig. 2d). The spectra of the unwashed MIP displayed characteristic absorption peaks at 1671 and 1612 cm-1 from C=N stretching and N-H bending/COO- asymmetric stretching respectively, which are attributable to L-Arginine and Methacrylic acid (MAA) interactions. The significant attenuation of these signature peaks in the washed MIP confirmed the successful and efficient elution of the template molecules, a crucial step for ensuring the availability of the binding cavities.

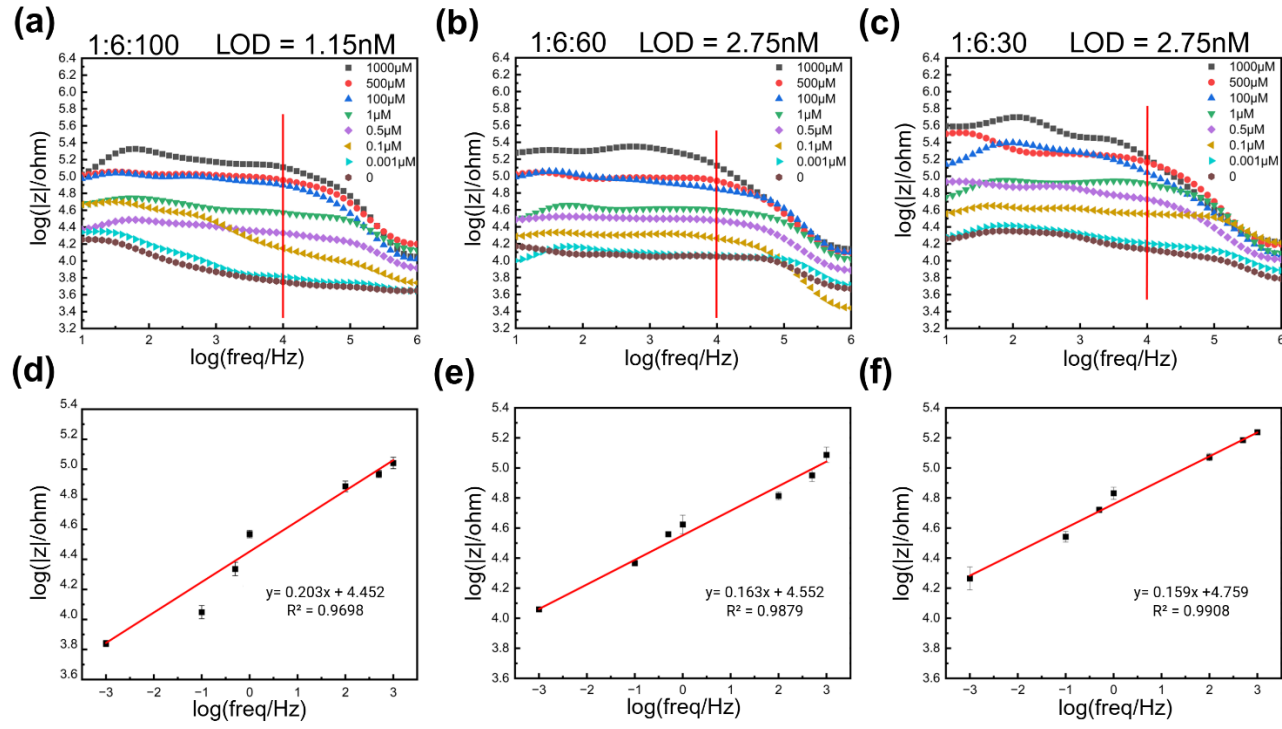
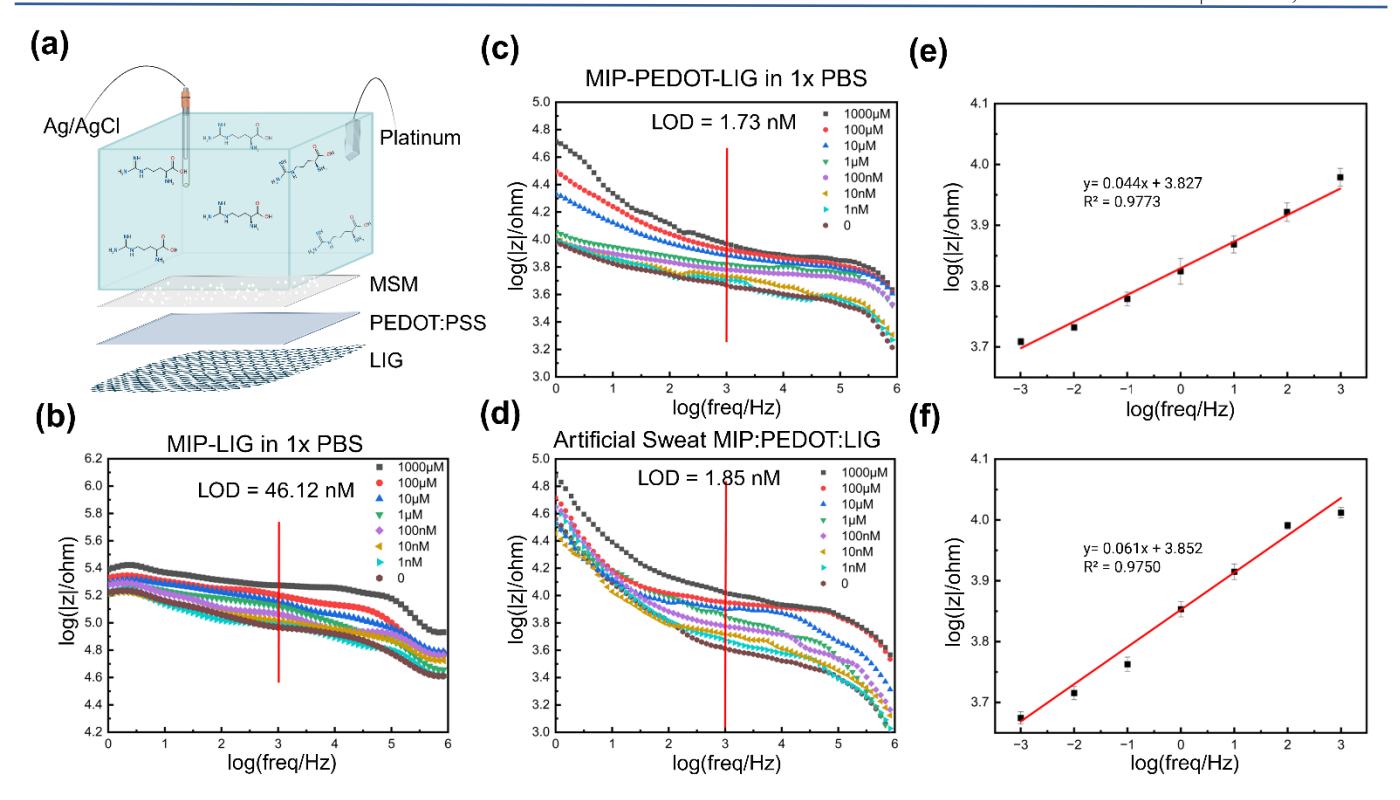


Figure 3. MIP Optimization based on testing from four-parallel connected MIP-PEDOT:PSS-LIG Electrodes using EIS. Each electrode was 200 micron in width and 1 cm in length. (a) MIP prepared from 1:6:100 (Arginine: MAA: EDMA) (template: monomer: crosslinker ratio) EIS from 1nM-1mM. (b) MIP 1:6:60 EIS from 1nM-1mM. (c) MIP 1:6:30 EIS from 1nM-1mM N=4. (d) MIP 1:6:100 EIS calibration curve. (e) MIP 1:6:60 EIS calibration curve N=4. (d) MIP 1:6:30 EIS calibration curve N=4.

#### 2.3 MIP Optimization

Sensitivity testing was then conducted to understand and optimize the MIP through Electrochemical Impedance Spectroscopy (EIS) over a frequency range of 1Hz to 1MHz. The impedance increased significantly with rising L-Arginine concentrations, confirming the sensor's responsiveness. The impedance of the device was analyzed throughout its modification process to better set an effective control. The frequency of 1 kHz was chosen for analysis, with the device demonstrating lower/improved impedance after PEDOT:PSS deposition (log|Z|  $\approx$  3.21 for PEDOT-LIG vs.  $\approx 3.38$  for LIG) (Fig. S6 in the ESM). Three distinct formulations were prepared with varying monomer-tocrosslinker molar ratios: 1:6:100, 1:6:60, and 1:6:30 as shown in (Fig. 3a), (Fig. 3b), and (Fig. 3c), respectively. The MIP synthesized with a template: monomer: crosslinker molar ratio at 1:6:100 demonstrated the lowest calculated LOD. Specifically, this formulation exhibited a marked and systematic increase in impedance upon exposure to escalating concentrations of L-Arginine from 1 nM to 1 mM with the lowest calculated LOD of 1.17 nM (Fig 3a). MIP 1:6:100 contains a high proportion of crosslinker to monomers, which should facilitate the formation of a more densely crosslinked, more rigid, three-dimensional polymer network. This structural rigidity can more effectively set the functional monomers in a specific spatial orientation around the L-arginine template molecule and organize them for more optimal non-covalent interactions. Upon subsequent removal of the template, this high degree of structural integrity ensures that the resulting recognition cavities are preserved with high fidelity. In contrast, the MIP formulations with lower crosslinker content displayed progressively diminished sensing performance. The sensor based on the 1:6:60 ratio (Fig. 3b) showed a less pronounced impedance response to L-arginine, vielding a slightly poorer/higher LOD of 2.75 nM. Performance degraded substantially for the 1:6:30 formulation (Fig. 3c), which produced a weak and less consistent response, resulting in a LOD of 69.18 nM, suggesting that this formulation has insufficient crosslinking density [43]. While recognition sites are still formed during polymerization, the reduced structural support makes these sites less defined, which upon removal of the L-arginine template possesses greater conformational freedom which may lead to potential distortion. Overall, the MIP formulation of 1:6:100 was determined to be the most effective recognition element and was used for subsequent electrochemical experiments and the final sensor design.



**Figure 4.** EIS characterization and analytical performance of the LIG-based molecularly imprinted sensors. (a) Schematic illustration of the three-electrode electrochemical setup (MIP-PEDOT:PSS-LIG working electrode, platinum wire counter electrode, and Ag/AgCl reference electrode) utilized for EIS analysis through an MSM. (b) EIS bode plots of the MIP-LIG sensor (without PEDOT:PSS) upon exposure to arginine concentrations ranging from 1 nM to 1 mM in 1x PBS. (c) EIS bode plots of the optimized MIP-PEDOT:PSS-LIG sensor in 1x PBS. (d) Bode plots of the optimized MIP-PEDOT:PSS-LIG sensor evaluated in an artificial sweat matrix. The red vertical lines in (bd) indicate the selected characteristic frequency (1 kHz; log(freq/Hz) = 3) for quantitative analysis. (e) Calibration curve derived from the data in (c) at 1 kHz in PBS (R² = 0.98). (f) Calibration curve derived from the data in (d) at 1 kHz in artificial sweat (R² = 0.98), N=4. The incorporation of PEDOT:PSS significantly enhanced sensor performance, lowering the calculated LOD from 46.12 nM (MIP-LIG) to 1.73 nM (MIP-PEDOT:PSS-LIG) N=4. Error bars in (e) and (f) represent the standard deviation of the measurements.

#### 2.4 Arginine Detection

Next, we employed EIS as a label-free transduction method to investigate the interfacial properties of the sensor modifications and to quantify L-Arginine binding events. Measurements were conducted using a conventional three-electrode system, as illustrated in Fig. 3a, with a Platinum (Pt) counter electrode and Ag/AgCl as a reference. The sensing mechanism for this type of sensor is well established that as the target analyte molecules occupy specific recognition cavities within the MIP layer, ionic transport gets impeded and hinders charge transfer, consequently increasing the measured impedance through the membrane.

To test sensing capabilities, we first tested LIG and found slight inter- electrode variety and a higher LOD, which necessitates the subsequent deposition of PEDOT:PSS, an electroconductive polymer which facilitates ion transfer with the MIP, enhancing the electrochemical transduction capabilities (lower LOD), improving signal stability, and improving batch-tobatch stability. The contribution of the conductive polymer interlayer was evaluated by comparing the impedance spectra of the MIP-LIG electrode (Fig. 3b) and the MIP-PEDOT:PSS-LIG electrode (Fig. 3c) in 1x PBS. The incorporation of PEDOT:PSS resulted in a substantial reduction in the overall impedance of the device. Specifically, at a frequency of 1 kHz (log(freq/Hz) = 3), the baseline impedance (at a concentration of 0) decreased substantially from approximately 10<sup>5.15</sup> for the MIP-LIG sensor to 10<sup>3.7</sup> for the MIP-PEDOT:PSS-LIG sensor. The subsequent enhancement in LOD is a result from the more efficient charge transfer kinetics at the electrode interface facilitated by PEDOT:PSS, leading to improved electrochemical performance. Crucially, this improvement translated to a significant enhancement in analytical sensitivity. The calculated LOD for the MIP-LIG sensor was 46.12 nM. In contrast, the optimized MIP-PEDOT:PSS-LIG sensor achieved a substantially lower LOD of 1.73 nM, representing a greater than 25-fold improvement in detection capability.

Fig. 3c displays the impedance plots for the optimized MIP-PEDOT:PSS-LIG sensor when exposed to analyte concentrations ranging from 1 nM to 1 mM in 1x PBS. A systematic, concentration-dependent increase in the impedance magnitude, was observed across the measured frequency spectrum, confirming the successful binding of the analyte within the MIP cavities, with higher concentration leading to increased impedance. To assess the sensor's applicability in complex biological fluids, its performance was evaluated in artificial sweat (Fig. 3d). The impedance trends closely mirrored those observed in the idealized PBS buffer, demonstrating the robustness and inherent selectivity of the MIP layer in a physiologically relevant medium, with minimal interference from the matrix components.

For quantitative analysis, 1 kHz was selected as the optimal operating frequency, as it demonstrated a significant and stable impedance response to changes in analyte concentration (indicated by the red vertical lines). Calibration curves were generated by plotting the logarithm of the impedance magnitude against the logarithm of the analyte concentration. The MIP-PEDOT:PSS-LIG sensor exhibited excellent linearity over a wide dynamic range spanning six orders of magnitude (1 nM to 1 mM). In 1x PBS (Fig. 3e) with a high coefficient of determination ( $R^2 = 0.98$ ) and an LOD of 1.73 nM. When tested in artificial sweat (Fig. 3f), the sensor maintained strong linearity ( $R^2 = 0.98$ ). These results validate the efficacy of the MIP-PEDOT:PSS-LIG platform for sensitive and reliable analyte detection in both standardized solutions and more complex artificial sweat.

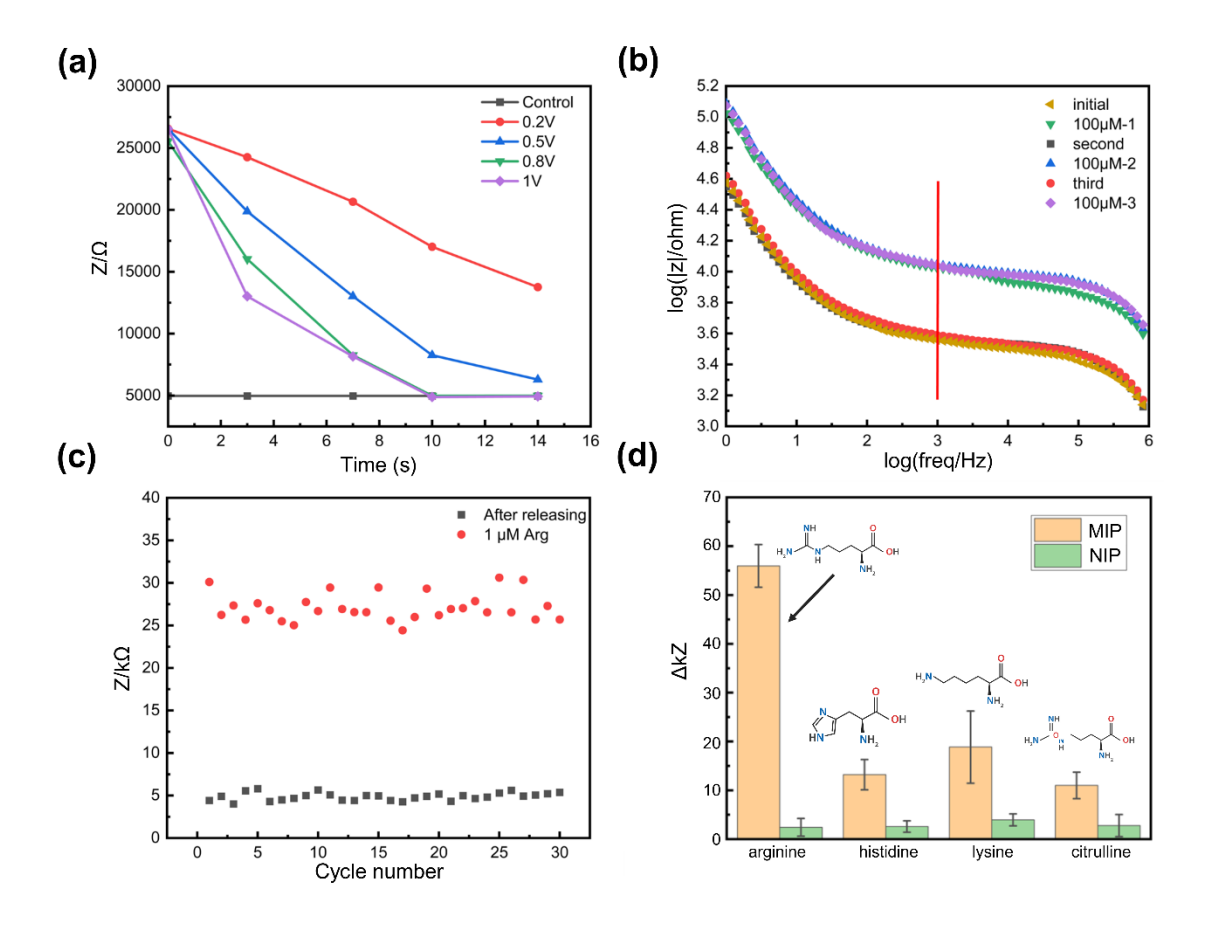


Figure 5. Electrostatic Release and Selectivity. (a) Bode amplitude measured at 1 kHz as a function of time after the voltage pulse for releasing is applied. Effect of pulse amplitude (0.2, 0.5, 0.8, and 1 V) and duration (2, 6, 8, 10, 14 s) on the releasing event after exposure to  $100 \,\mu\text{M}$  of arginine. (b) Reversibility of releasing by voltage pulse. A potential of  $0.8 \,\text{V}$  was applied for  $10 \,\text{seconds}$  to induce analyte repulsion. Impedance was measured and measured again after subsequent exposure to  $100 \,\mu\text{M}$  of arginine. This process is then repeated twice (second, third). Repeated reversibility with no discernable difference in sensing is observed. (c) Reversibility test by recording bode amplitude through EIS measured at  $1 \,\text{kHz}$  over  $30 \,\text{binding-releasing}$  cycles for the sensor in the presence of  $1 \,\mu\text{M}$  L-arginine. (d) Selectivity analysis of the sensor from the change in impedance ( $\Delta Z$ ) upon exposure to  $100 \,\mu\text{M}$  of arginine versus histidine, lysine, and citrulline. N=4.

#### 2.5 Reversibility and Selectivity

The long-term stability and reusability of the sensor are critical for continuous monitoring. Using a controlled electrostatic pulse to actively trigger analyte release, a rapid and non-destructive method, the sensors demonstrate an almost complete release and discernable variation to subsequent sensing measurements, achieving a similar result to Hemed et. al's work on reversible dopamine MIP sensors [50]. The parameters for the electrostatic release were optimized to maximize regeneration while minimizing applied potential and time. This optimization involved testing a variety of pulse amplitudes (0.2, 0.5, 0.8, and 1.0 V) following sensor saturation with 100 µM L-arginine across various durations (2 to 14 s) (Fig. 5a). The voltages were selected based on potential release mechanisms. Regeneration under lower potentials (e.g.,  $\leq 0.2 \text{ V}$ ) would indicate the presence of primarily electrostatic repulsion of the positively charged L-arginine. Conversely, potentials exceeding 0.5 V would be approaching the threshold for direct electrochemical oxidation governed by the Butler-Volmer equation of L-arginine. The results successfully demonstrated sensor regeneration using a potential of 0.8 V applied for 10 seconds to achieve near-complete analyte release (>98% signal recovery). The reversibility of the sensor under these optimized conditions was further evaluated using EIS. As depicted in Fig. 5b, re-exposure to L-arginine (100 µM) induced

an expected significant shift in the impedance spectra due to the analyte binding within the MIP cavities. Upon application of the optimized regeneration pulse (0.8 V for 10 s), the impedance signal consistently returned to its initial baseline within approximately 15 seconds. This process was repeated for two consecutive exposure and regeneration cycles (Exposures 1, 2, and 3; initial, second, and third) to demonstrate successful repeated reversibility with no discernible difference in sensing. The negligible variation observed in both the binding sensitivity and the baseline recovery across these cycles confirms the potential for continuous, rapid electrochemical reversibility of the platform. To further assess long-term operational stability, the sensor was subjected to 30 continuous binding-releasing cycles in the presence of 1 µM L-arginine (Fig. 5c). Each cycle comprised a 5-minute incubation period to allow for binding, followed by the 10-second electrostatic release pulse. The Bode amplitude was monitored at 1 kHz throughout the 30 cycles. The impedance signal reliably returned to the baseline following each regeneration step, indicating analyte desorption with no discernible memory effect or significant signal drift. This stability confirms that neither the MIP recognition layer nor the underlying LIG electrode suffered notable degradation during repeated electrochemical pulsing. This high degree of reusability is critical for the integration into wearable devices through facilitating

continuous or semi-continuous monitoring. Furthermore, selectivity is critical for a biosensor to function reliably within a complex biofluid such as sweat. The selectivity of the sensor was tested against three biologically relevant and structurally analogous amino acids (lysine (Lys), histidine (His), and citrulline (Cit)) through EIS. The sensor was exposed to 100 µM of each molecule for 10 minutes and its impedance change was recorded (ΔZ) and compared to a response elicited by an equimolar concentration of L-arginine (Fig. 5d). This selection of amino acids was intentional, as Lysine and histidine are structurally similar to arginine, the only significant structural difference being the side chain. Instead of L-Arg's guanidinium group, Lys possesses an ε-amino group and His possesses an imidazole ring, both of which could potentially interact nonspecifically with faulty MIP cavities. Furthermore, Citrulline is the direct metabolic product of arginine, warranting interest due to its shared biological relationship, and holds further structural homology. The results demonstrate pronounced selectivity; the impedance change ( $\Delta Z$ ) upon exposure to L-arginine was approximately three-fold higher than the response generated by any of the interfering amino acids. This differential response confirms that the selectivity of the sensor's recognition mechanism is not simply based on non-specific electrostatic attraction and stands as an important step towards discerning specific biomolecules through sweat in a wearable device.

# 3 Conclusion

Our work successfully demonstrated the fabrication of a selective and sensitive L-arginine MIP-based sensor on a PEDOT:PSS deposited laser-induced graphene electrode on a flexible polyimide substrate. The PEDOT:PSS coating was found to decrease impedance and improve sensitivity. Our fabricated sensor showed high sensitivity and selectivity toward its target analyte, more than covering the physiologically relevant range of L-arginine in human sweat (1nM-1mM). Our sensor provides a potential point-of-care alternative to traditional lab-based blood analysis. When incorporated into wearable devices, they offer significant promise for benefits in accessibility and continuous monitoring. Future work will focus on in vivo testing, integration of a sensor array for other biomarkers like L-Citrulline and L-Ornithine, and development of a complete system with miniature, embedded wireless electronics.

# 4 Methods

#### 4.1 Materials

L-Arginine (Sigma), Methacrylic acid (MAA) (Sigma), Ethylene Glycol Dimethacrylate (EDMA) (Ambeed), 2,2'-azobis(2-methylpropionitrile) (AIBN) (Sigma), Dioctyl Phthalate (Sigma), tetrahydrofuran (THF), Potassium tetrakis(4-chloropheny1) borate (Sigma), Poly(vinyl chloride) (PVC) (Sigma), 2,3-Dihydrothieno[3,4-b][1,4]dioxine (Ambeed), Lithium Perchlorate (Sigma), Poly(sodium 4-styrenesulfonate) (Sigma), Acetonitrile, Trifluoroacetic acid (Sigma), Methanol, DI Water, Silver Paste, Polyimide (Kapton), Epoxy (Torr Seal®), and 1× PBS solution were purchased from Fisher BioReagents. Working standard solutions were prepared fresh daily. All solvents were of either analytical or HPLC grade.

# 4.2 SEM Parameters

Instrument Model: Zeiss Sigma 360. Spectrometer: Oxford Azteclivelite Ultimax 40. We applied approximately 10 mg of MIP powder directly to the conductive adhesive for testing

### 4.3 BET Parameters

BET: Instrument model: Mac ASAP2460. For nitrogen adsorption, as the specific surface area was still unknown, the mass for testing the full pore and micropore mode used was over 100 mg, with over 250 mg required for testing in the mesopore mode.

#### 4.4 ITC Parameters

The test concentration of L-Arginine used for ITC was 20 mg/ml with a 2 mg/ml concentration of MIP/NIP. The initial volume of the L-arginine solution titrated was 50  $\mu$ l (drawn into the syringe) with an initial volume of the MIP/NIP solution of 300  $\mu$ l (added to the sample cell). 20 drops of 2  $\mu$ l of solution were added dropwise, with a titration interval of 120 seconds, a temperature of 25°C, and a stirring speed of 350 rpm.

#### 4.5 FT-IR Parameters

Instrument Model: Bruker INVENIO S. FT-IR was conducted with both the MIPs and NIPs using a Bruker INVENIO S by mixing a small amount of powdered sample with potassium bromide, pressing the compound into a pellet, and placing it on a universal attenuated total reflectance (ATR) sample accessory.

# 4.6 MIP Synthesis

10 mL of unacidified acetonitrile was poured into a 250 mL round-bottom flask with a subsequent addition of 20.2 mg of template (L-arginine). To improve the solubility of L-arginine in acetonitrile, 40 µL of trifluoroacetic acid was added dropwise, and a 1:6:100 molar ratio of template to monomer (MAA) to crosslinker (EDMA) was added to the solution, followed by sonication for 10 minutes to completely dissolve the template. After sonication, the mixture was allowed to sit at room temperature for about 5 minutes to rest, and then 20.0 mg of initiator 2,2'azobisisobutyronitrile (AIBN) was added. The solution was than purged with nitrogen for 7 minutes and then closed entirely with a glass stopper and wrapped with parafilm tape. The reaction flask was then immersed in an oil bath placed on a hot plate set at 60°C to start the polymerization reaction through thermal initiation. After 24 hours of polymerization, the MIPs were removed from the flask and dried under vacuum at 60 °C to remove any residual chemicals. The dried polymer was then mechanically crushed, ground in a mortar, and sieved on a 47 µM pore sieve to obtain a fine powder. The powder was then loaded into a thimble, and the template was removed from the MIP using a Soxhlet apparatus for overnight washing cycles with methanol. After washing, the MIP powder was again dried in a vacuum oven for twenty-four hours at 60 degrees Celsius. The dried MIP's composition consistency was monitored using FT-IR Spectroscopy. The nonimprinted polymer (NIP) was prepared and treated in a similar manner as described above, except the template (L-arginine) was not included in the reaction mixture.

#### 4.7 MSM Preparation

The selective membrane was prepared by dissolving 51.0 mg of PVC, 120.0  $\mu$ L of bis(2ethylhexyl) phthalate, and 15.0 mg of potassium tetrakis(4-chlorophenyl) borate in 2 mL of THF. The arginine MIP was then dispersed into this solution using a 5 mg/ml ratio.

# 4.8 Sensor Preparation

Sensor fabrication began with laser engraving of 100-micron LIG electrodes under a 6-watt CO2 laser to pyrolyze polyimide. Afterward, each sensor was connected to a copper tape. Silver paste was then applied on the connections area followed by drying on a hot plate set at 60°C for 15 minutes. Further strengthening of the sensor using Polyimide (Kapton) tape was done, with

complete coverage except for the connection areas and electrode/sensor tips. The connection areas were then reinforced with Kapton tape and epoxy (Torr Seal®). The molecularly selective layer was coated on top of electropolymerized PEDOT:PSS by dip coating into a mixture of tetrahydrofuran (2 mL) containing MIPs (concentration), high molecular weight PVC (51.0 mg), bis(2-ethylhexyl) plasticizer solvent medium (120.0 L), and anion excluder tetrakis(4-chlorophenyl)borate (15.0 mg). The sensors were dried overnight at ambient temperature under vacuum conditions.

#### 4.9 PEDOT:PSS Electrodeposition

Electrodeposition of PEDOT:PSS on LIG was conducted to increase overall electrode conductivity and lower impedance. Electrodeposition was performed using a PalmSens4 potentiostat in a three-electrode setup with the encapsulated LIG sensor as the working electrode, a Platinum counter electrode (CE), and a commercial? silver/silver chloride (Ag/AgCl) reference electrode (RE). A 6 ml solution of 10 mM 3,4-Ethylenedioxythiophene (EDOT) and 0.1 mM poly(sodium-4-styrenesulfonate) (NaPSS) containing 0.1 M Lithium Perchlorate (LiClO4) in a solvent mixture of DI water/Acetonitrile (1:1 v/v) was created. The PEDOT:PSS electropolymerization was performed using Cyclic voltametric (CV) at -0.8 to 1.8V at 50 mV/s for 10 cycles in the solution. The sensor was then subsequently dip-coated in the membrane solution, allowed to sit in ambient air for 30 minutes, and then subjected to overnight drying under vacuum conditions at 60°C using a house vacuum.

## 4.10 EIS Testing Parameters

EIS measurements were performed using a PalmSens4 Potentiostat with the MIP-PEDOT:PSS-LIG sensor as the working electrode, a platinum electrode as a counter and an Ag/AgCl reference electrode. Impedance characteristics were performed in the frequency range 1 Hz-1 mHz using a potentiostat. The electrolyte used was 10 mL of PBS 1x solution at pH = 7.45 at room temperature. For the sensitivity testing, parameters of 1Hz-1mHz, 31=5/dec n frequencies, fixed scan were used, with the electrolyte being an L-arginine solution in a concentration range of 1 nM - 1mM. The measurement protocol included an initial equilibration period of 5 minutes followed by five consecutive impedance measurements. Testing was first conducted without L-arginine to establish a baseline, then incrementally adjusted by adding various concentrations of the analyte solution respectively, with the impedance measurements repeated after each concentration adjustment.

#### 4.11 Reversibility/Arginine Release

Reversibility validation was performed using a conventional three-electrode-cell setup with our device as the working electrode, a platinum metal counter electrode, and an Ag/AgCl reference electrode. A small potential step was then applied with an amplitude of 0.8 V and duration of 10s.

Electronic Supplementary Material: The Supporting Information is available free of charge. Experimental procedures and characterization data are available online is available in the online version of this article at http://dx.doi.org/10.1007/s12274-\*\*\*-\*\*\*-\*

(automatically inserted by the publisher). Figures

(automatically inserted by the publisher). Figures detailing SEM characterization (top-view and cross-sectional) of PEDOT:PSS morphology; optimization of PEDOT:PSS electrodeposition cycles for impedance reduction; Raman spectroscopy of the laser-induced

graphene (LIG) electrode; SEM analysis of MIP and NIP nanosphere agglomerates; comparative analysis of MIP and NIP surface topography and BET specific surface area; Isothermal Titration Calorimetry (ITC) data for the NIP; BJH analysis detailing average nanoparticle size and MIP pore diameter; and impedance analysis characterizing the different stages of device modification (PEDOT:PSS deposition and MSM integration).

# **Data availability**

All data needed to support the conclusions in the paper are presented in the manuscript and/or the Electronic Supplementary Material. Additional data related to this paper may be requested from the corresponding author upon request.

# Acknowledgements

R.G. acknowledges Eric Z. and Jeffery Tok for helpful discussions and support. The authors declare no conflict of interest. This research was supported by Stanford Wearable Electronics Initiative (eWEAR).

# **Declaration of competing interest**

All the contributing author(s) report(s) no conflict of interests in this work

# **Author contribution statement**

R.G.: Experimental design, data curation, conducted experimentation, writing manuscript, conceptualization. M.K.: validation, review for the manuscript. K-J.H.: Conducted characterization work (SEM, etc), review for the manuscript. Z.B.: Editing and reviewing the manuscript, project administration. All authors have approved the final manuscript

# **Informed consent**

Not Applicable

# **Ethics statement**

Not applicable.

# Use of AI statement

None

#### References

- Kim, J.; Campbell, A. S.; de Ávila, B. E. F.; Wang, J. Wearable biosensors for healthcare monitoring. *Nat. Biotechnol.* 2019, 37, 389– 406.
- [2] Zhao, C.; Park, J.; Root, S. E.; Bao, Z. Skin-inspired soft bioelectronic materials, devices and systems. *Nat. Rev. Bioeng.* 2024, 2, 671–690.
- [3] Min, J.; Tu, J.; Xu, C.; Lukas, H.; Shin, S.; Yang, Y.; Solomon, S. A.; Mukasa, D.; Gao, W. Skin-interfaced wearable sweat sensors for precision medicine. *Chem. Rev.* 2023, 123, 11213–11267.
- [4] Wang, B.; Zhao, Y.; Zhong, Z.; Zhang, G.; Wang, Y.; Xu, K.; Ye, Y.; Zhou, Y.; Yang, C.; Chen, Y. et al. Wearable aptamer-field-effect transistor sensing system for noninvasive cortisol monitoring. Sci. Adv. 2022, 8, eabk0967.
- [5] Wang, M.; Yang, Y.; Min, J.; Song, Y.; Tu, J.; Mukasa, D.; Yeung, C.; Xu, C.; Gao, W. A wearable electrochemical biosensor for the monitoring of metabolites and nutrients. *Nat. Biomed. Eng.* 2022, 6, 1225–1235.
- [6] McPartlin, D. A.; O'Kennedy, R. J. Point-of-care diagnostics, a major opportunity for change in traditional diagnostic approaches: Potential and limitations. *Expert Rev. Mol. Diagn.* 2014, 14, 979–998.
- [7] Wu, J.; Liu, H.; Chen, W.; Zhou, L. Device integration of

- electrochemical biosensors. Nat. Rev. Bioeng. 2023, 1, 346-360.
- [8] Sempionatto, J. R.; Lasalde-Ramírez, J. A.; Mahato, K.; Wang, J.; Gao, W. Wearable chemical sensors for biomarker discovery in the omics era. *Nat. Rev. Chem.* 2022, 6, 899–915.
- [9] Ma, C.-B.; Shang, X.; Sun, M.; Zhang, C.; Zhang, Q. Emerging multifunctional wearable sensors: Integrating multimodal sweat analysis and advanced material technologies for next-generation health monitoring. ACS Sens. 2025. 10, 2388-2406.
- [10] Yang, D. S.; Ghaffari, R. Sweat as a diagnostic biofluid. *Science* 2023, 379, 760–761.
- [11] Zhang, Z.; Li, Z.; Wei, K.; Wang, X. Sweat as a source of non-invasive biomarkers for clinical diagnosis: An overview. *Talanta*. 2024, 273, 125865.
- [12] Gao, F.; Liu, C.; Zhang, L.; Liu, K. Wearable and flexible electrochemical sensors for sweat analysis: A review. *Microsyst. Nanoeng.* 2023, 9, 1.
- [13] Martinez-Reyes, I.; Chandel, N. S. Mitochondrial TCA cycle metabolites control physiology and disease. *Nat. Commun.* 2020, 11, 102
- [14] Klaessens, S.; Stroobant, V.; De Plaen, E.; Van den Eynde, B. Systemic tryptophan homeostasis. Front. Mol. Biosci. 2022, 9, 897929.
- [15] Lieu, E. L.; Nguyen, T.; Rhyne, S.; Kim, J. Amino acids in cancer. Exp. Mol. Med. 2020, 52, 15–30.
- [16] Gałezowska, G.; Ratajczyk, J.; Wolska, L. Determination of amino acids in human biological fluids by high-performance liquid chromatography: critical review. *Amino Acids* 2021, 53, 993–1009.
- [17] Spano, J.; Demchak, L.; Nakano, K.; Conti, T.; Heikenfeld, J.; Milla, C. Investigation of effects of collection conditions on amino acid concentrations in sweat and correlations with their Circulating levels in plasma. *Sci Rep.* 2025, 15, 23198.
- [18] Kuroki, H.; Tsunoda, M. Quantification of amino acids in small volumes of human sweat collected from fingertips of healthy subjects at rest. J. Pharm. Biomed. Anal. 2025, 257, 116718.
- [19] Gupta, M. N.; Uversky, V. N. Biological importance of arginine: A comprehensive review of the roles in structure, disorder, and functionality of peptides and proteins. *Int. J. Biol. Macromol.* 2024, 257, 128646.
- [20] Reyes, A. A.; Karl, I. E.; Klahr, S. Role of arginine in health and in renal disease. Am. J. Physiol. 1994, 267, F331–F346.
- [21] Canè, S.; Geiger, R.; Bronte, V. The roles of arginases and arginine in immunity. *Nat. Rev. Immunol.* 2025, 25, 266–284.
- [22] O'Shaughnessy, R. F. L. Adding arginine to the list of single amino acids important in epidermal barrier function. *Br. J. Dermatol.* 2025, 193, 7–8.
- [23] Tousoulis, D.; Böger, R.; Antoniades, C.; Siasos, G.; Stefanadis, C. Mechanisms of disease: L-arginine in coronary atherosclerosis—a clinical perspective. *Nat. Rev. Cardiol.* 2007, 4, 274–283.
- [24] Wu, G.; Meininger, C. J.; McNeal, C. J.; Bazer, F. W.; Rhoads, J. M. Role of L-arginine in nitric oxide synthesis and health in humans. In Amino Acids in Nutrition and Health; Springer: Cham, 2021; pp 167– 187
- [25] Molek, P.; Zmudzki, P.; Wlodarczyk, A.; Krol, J. The shifted balance of arginine metabolites in acute myocardial infarction patients and its clinical relevance. *Sci. Rep.* 2021, 11, 83.
- [26] Hecker, M.; Sessa, W. C.; Harris, H. J.; Anggard, E. E.; Vane, J. R. The metabolism of L-arginine and its significance for the biosynthesis of endothelium-derived relaxing factor: Cultured endothelial cells recycle L-citrulline to L-arginine. *Proc. Natl. Acad. Sci. U.S.A.* 1990, 87, 8612–8616.
- [27] Jiang, H.; Zhou, Y.; Nabavi, S. M.; Sahebkar, A.; Little, P. J.; Xu, S.; Weng, J.; Ge, J. Mechanisms of oxidized LDL-mediated endothelial dysfunction and its consequences for the development of atherosclerosis. Front. Cardiovasc. Med. 2022, 9, 925923.
- [28] Ambrosino, P.; Bachetti, T.; D'Anna, S. E.; Cacciatore, F. Mechanisms and clinical implications of endothelial dysfunction in arterial hypertension. *J. Cardiovasc. Dev. Dis.* 2022, 9, 136.
- [29] Förstermann, U.; Münzel, T. Endothelial nitric oxide synthase in vascular disease. Circulation 2006, 113, 1708–1714.
- [30] Gawrys, J.; Gajecki, D.; Szahidewicz-Krupska, E.; Doroszko, A. Intraplatelet L-arginine-nitric oxide metabolic pathway: From discovery to clinical implications in prevention and treatment of

- cardiovascular disorders. Oxid. Med. Cell. Longev. 2020, 2020, 1015908
- [31] Goumas, G.; Tentolouris, C.; Tousoulis, D.; Stefanadis, C.; Toutouzas, P. Therapeutic modification of the L-arginine-eNOS pathway in cardiovascular diseases. *Atherosclerosis* 2001, 154, 255– 267
- [32] Oyovwi, M. O.; Atere, A. D. Exploring the medicinal significance of L-arginine mediated nitric oxide in preventing health disorders. Eur. J. Med. Chem. Rep. 2024, 12, 100175.
- [33] Verma, N.; Singh, A. K.; Kaur, P. Biosensor based on ion selective electrode for detection of L-arginine in fruit juices. *J. Anal. Chem.* 2015, 70, 1111–1115.
- [34] Zhybak, M. T.; Fayura, L. Y.; Boretsky, Y. R.; Gonchar, M. V.; Sibirny, A. A.; Dempsey, E.; Turner, A. P. F.; Korpan, Y. I. Amperometric L-arginine biosensor based on a novel recombinant arginine deiminase. *Microchim. Acta* 2017, 184, 2679–2686.
- [35] Komaba, S.; Fujino, Y.; Matsuda, T.; Osaka, T.; Satoh, I. Biological determination of Ag(I) ion and arginine by using the composite film of electroinactive polypyrrole and polyion complex. Sens. Actuators B Chem. 1999, 52, 78–83.
- [36] Sheliakina, M.; Arkhypova, V.; Soldatkin, O.; Saiapina, O.; Akata, B.; Dzyadevych, S. Urease-based ISFET biosensor for arginine determination. *Talanta* 2013, 121, 18–23.
- [37] Pandey, S. P.; Singh, P. K. A polyelectrolyte based ratiometric optical sensor for arginine and lysine. *Sens. Actuators B Chem.* 2019, 303, 127182.
- [38] Tasić, T.; Milanković, V.; Pašti, I. A.; Lazarević-Pašti, T. Harnessing molecularly imprinted polymers as artificial antibodies in electrochemical sensors for disease detection and monitoring. In Molecularly Imprinted Polymers: Path to Artificial Antibodies; Springer, 2024.
- [39] Verma, N.; Singh, A. K.; Singh, M. L-arginine biosensors: A comprehensive review. *Biochem. Biophys. Rep.* 2017, 12, 228–239.
- [40] Wang, L.; Zhang, W. Molecularly imprinted polymer (MIP) based electrochemical sensors and their recent advances in health applications. Sens. Actuators Rep. 2023, 5, 100153.
- [41] BelBruno, J. J. Molecularly imprinted polymers. Chem. Rev. 2018, 119, 94–119.
- [42] Sengar, M. S.; Kumari, P.; Sengar, N.; Singh, S. K. Molecularly imprinted polymer technology for the advancement of its health surveillances and environmental monitoring. ACS Appl. Polym. Mater. 2024, 6, 1086–1105.
- [43] Li, Z.; Huang, L.; Cheng, L.; Guo, W.; Ye, R. Laser-induced graphene-based sensors in health monitoring: Progress, sensing mechanisms, and applications. *Small Methods* 2024, 8, 2400118.
- [44] Mu, M.; Chen, G.; Yu, W.; Liu, J.; Wang, Y. In situ growth of laser-induced graphene on flexible substrates for wearable sensors. ACS Appl. Nano Mater. 2024, 7, 3279–3288.
- [45] Huang, Q.; Dai, X.; Guo, S.; Ma, S.; Zhao, C.; Su, W. Flexible, wearable and sensitive laser-induced graphene sensors for human health monitoring. *Polym. Adv. Technol.* 2024, 35, 6473.
- [46] Mbukwa, E. A.; Titus; Mamba, B. B. Preparation of guanidinium terminus-molecularly imprinted polymers for selective recognition and solid-phase extraction (SPE) of [arginine]-microcystins. *Anal. Bioanal. Chem.* 2013, 405, 4253–4267.
- [47] Weber, A.; Dettling, M.; Brunner, H.; Tovar, G. E. M. Isothermal titration calorimetry of molecularly imprinted polymer nanospheres. *Macromol. Rapid Commun.* 2002, 23, 824–828.
- [48] Wu, L.; Gao, Y.; Wang, J. Synthesis, application, and molecular recognition mechanism study of phenylalanine molecularly imprinted polymer. *Anal. Lett.* 2007, 40, 3129–3147.
- [49] Golker, K.; Nicholls, I. A. The effect of crosslinking density on molecularly imprinted polymer morphology and recognition. *Eur. Polym. J.* 2016, 75, 423–430.
- [50] Hemed, N. M.; Leal-Ortiz, S.; Zhao, E. T.; Melosh, N. A. On-demand, reversible, ultrasensitive polymer membrane based on molecular imprinting polymer. ACS Nano 2023, 17, 5632–5643.
- © The Author(s) 20xx. Nano Research published by Tsinghua University Press. The articles published in this open access journal are distributed under the terms of the Creative Commons Attribution 4.0 International License (http://creativecommons.org/licenses/by/4.0/), which permits use, distribution and reproduction in any medium, provided the original work is properly cited.

# **Electronic Supplementary Material**

# Supplemental Information: Arginine-Specific Molecularly Imprinted Polymer-Based Laser-Induced Graphene Flexible Sensor

Ruotong Gao¹, Muhammad Khatib¹, Kuang-Jung Hsu¹, and Zhenan Bao¹ <sup>™</sup>

Supporting information to https://doi.org/10.26599/NR.xxxx.949xxxxx (automatically inserted by the publisher)

<sup>&</sup>lt;sup>1</sup>Department of Chemical Engineering, Stanford University, Stanford, CA 94305, USA.

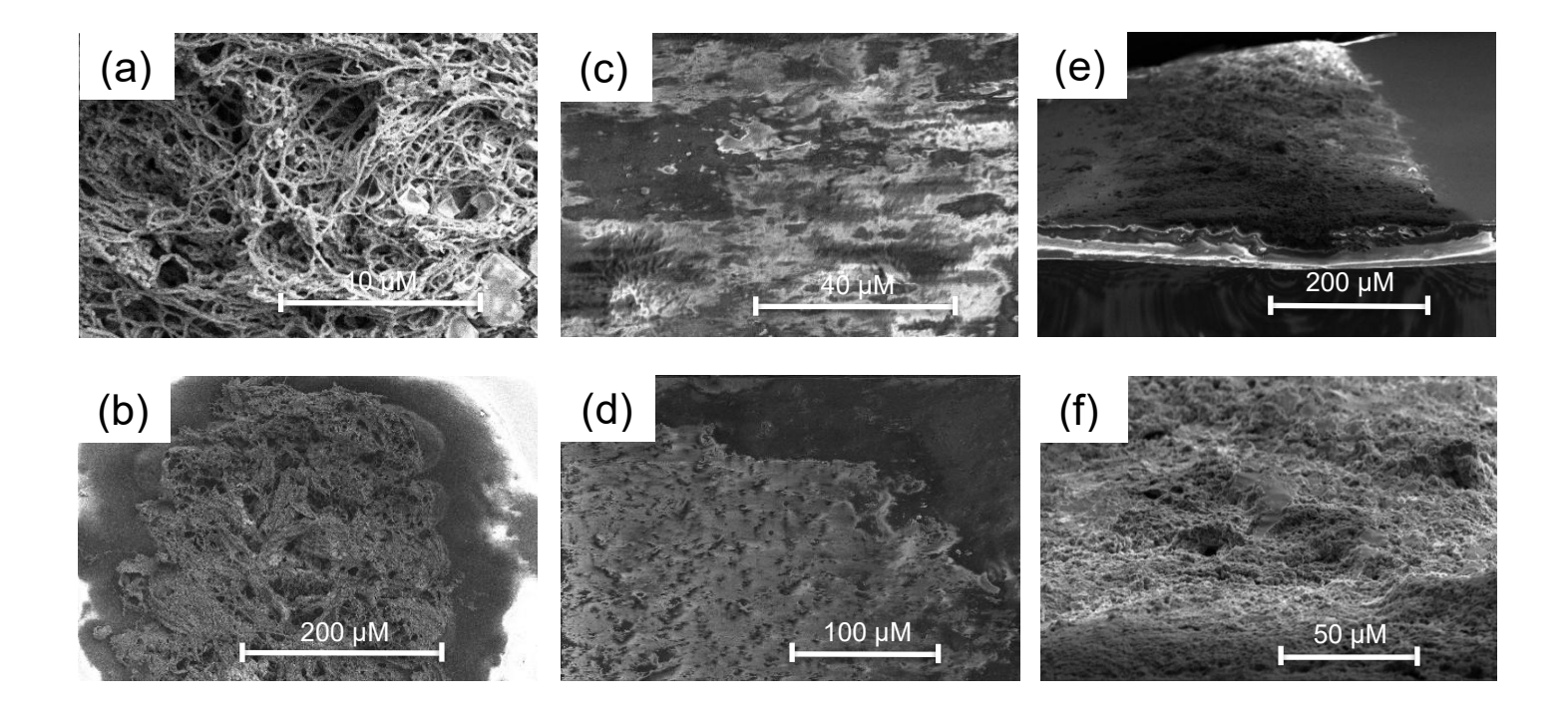


Figure S1. (a, b) Two representative SEM images of the LIG-PEDOT:PSS substrate prior to MIP deposition, revealing the architecture of the modified electrode. Top-down Scanning Electron Microscopy (SEM) visualization of the sensor surface morphologies. Fig S1. (c, d), Two representative SEM images of the complete LIG-PEDOT:PSS-MIP composite, illustrating the deposition of MIP particles on the surface of PEDOT:PSS-LIG. Fig S1 (e) shows the cross section of the PEDOT:PSS-LIG electrode, demonstrating a dark and bright layer of the PEDOT:PSS integrated with the LIG. Fig S1 (f) shows the cross-section of the LIG-PEDOT:PSS-MIP composite, visualizing the coverage of LIG with PEDOT:PSS and MIPs.

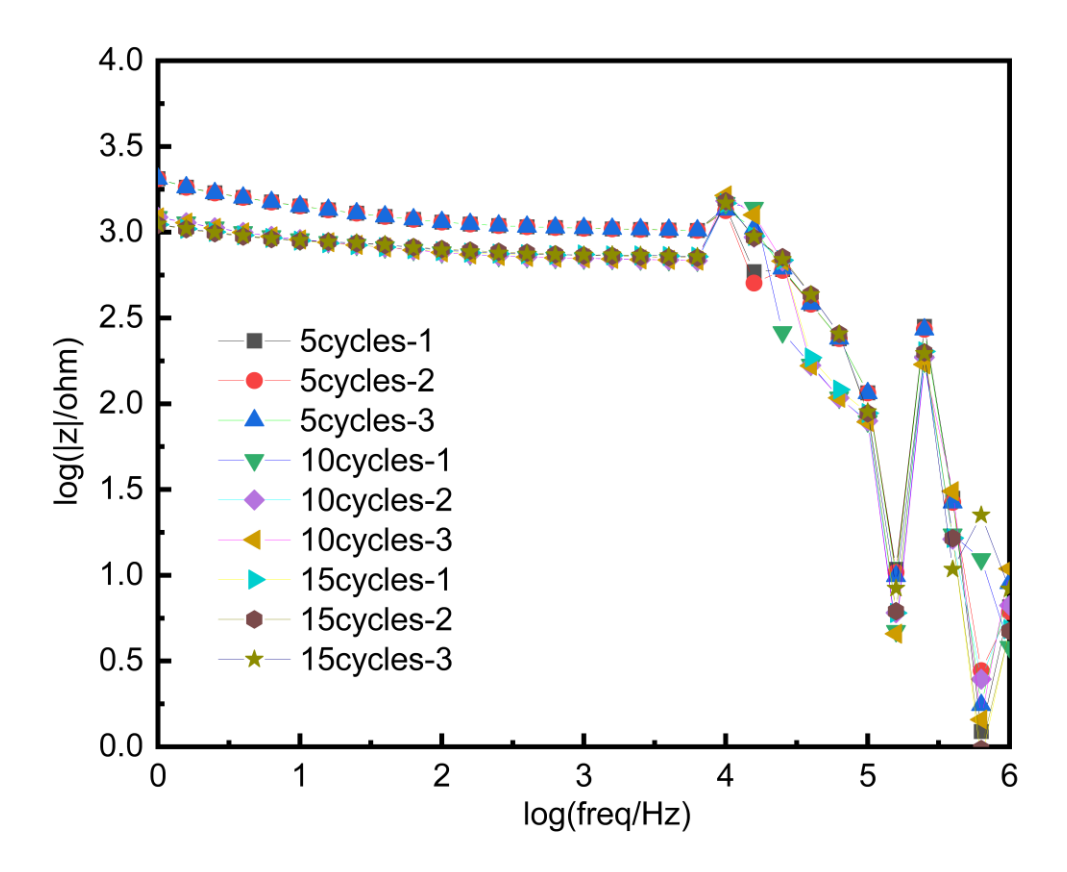


Figure S2. PEDOT:PSS Optimization from 5 cycles, 10 cycles, 15 cycles. Optimization of the PEDOT:PSS conductive polymer deposition process assessed by Electrochemical Impedance Spectroscopy (EIS). Bode plots (log|Z| vs. log(freq/Hz)) illustrate the electrochemical characteristics of electrodes fabricated using 5, 10, and 15 deposition cycles. Triplicate measurements (indicated as -1, -2, -3) for each condition demonstrate high reproducibility of the fabrication process and consistent impedance characteristics.

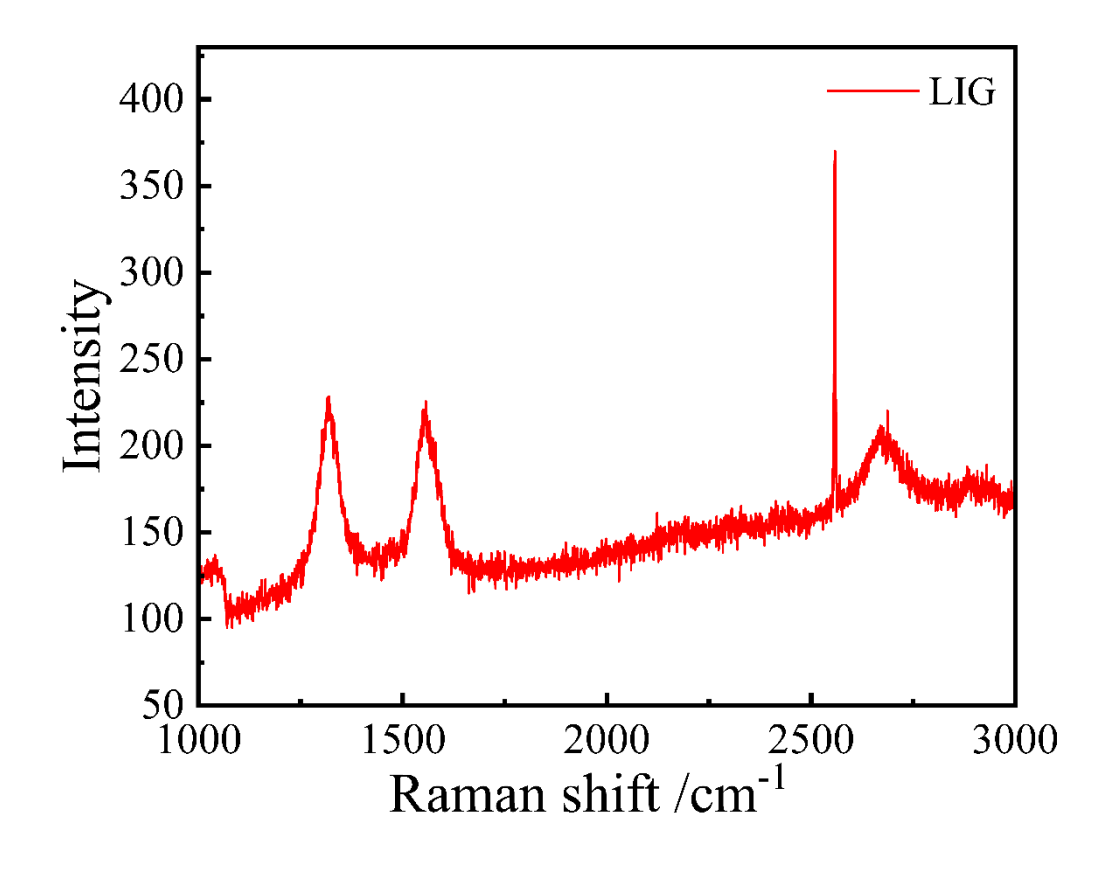


Figure S3. Raman spectroscopic characterization of the Laser-Induced Graphene (LIG) electrode substrate. The spectrum exhibits characteristic peaks of graphitic materials: the D band (~1350 cm<sup>-1</sup>), associated with defects or disordered carbon; the G band (~1580 cm<sup>-1</sup>), corresponding to the vibration of sp2-hybridized carbon atoms; and the 2D band (~2700 cm<sup>-1</sup>). The presence and profile of these peaks confirm the successful formation of multi-layered graphene structures during the laser induction process.

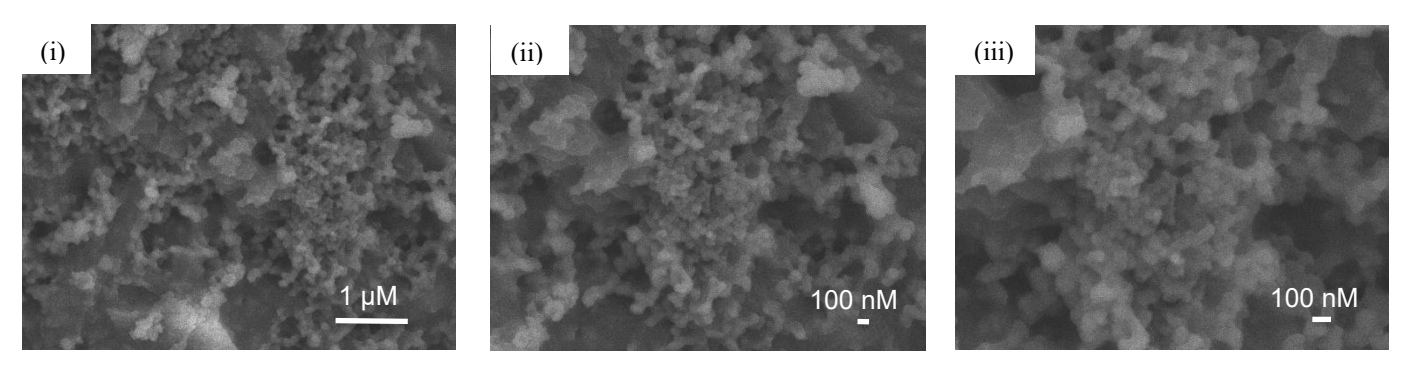


Figure S4. Scanning Electron Microscopy (SEM) images of the microstructure and surface morphology of the Non-Imprinted Polymer (NIP) particles. The micrographs reveal agglomerated structures composed of irregular nanoscale subunits. Images captured at increasing magnifications: (i) 20.00 K X (Scale bar: 500 nm), (ii) 50.00 K X (Scale bar: 200 nm), and (iii) 100.00 K X (Scale bar: 100 nm). Imaging conditions: EHT = 10.00 kV, WD = 5.1 mm, Signal A = InLens.

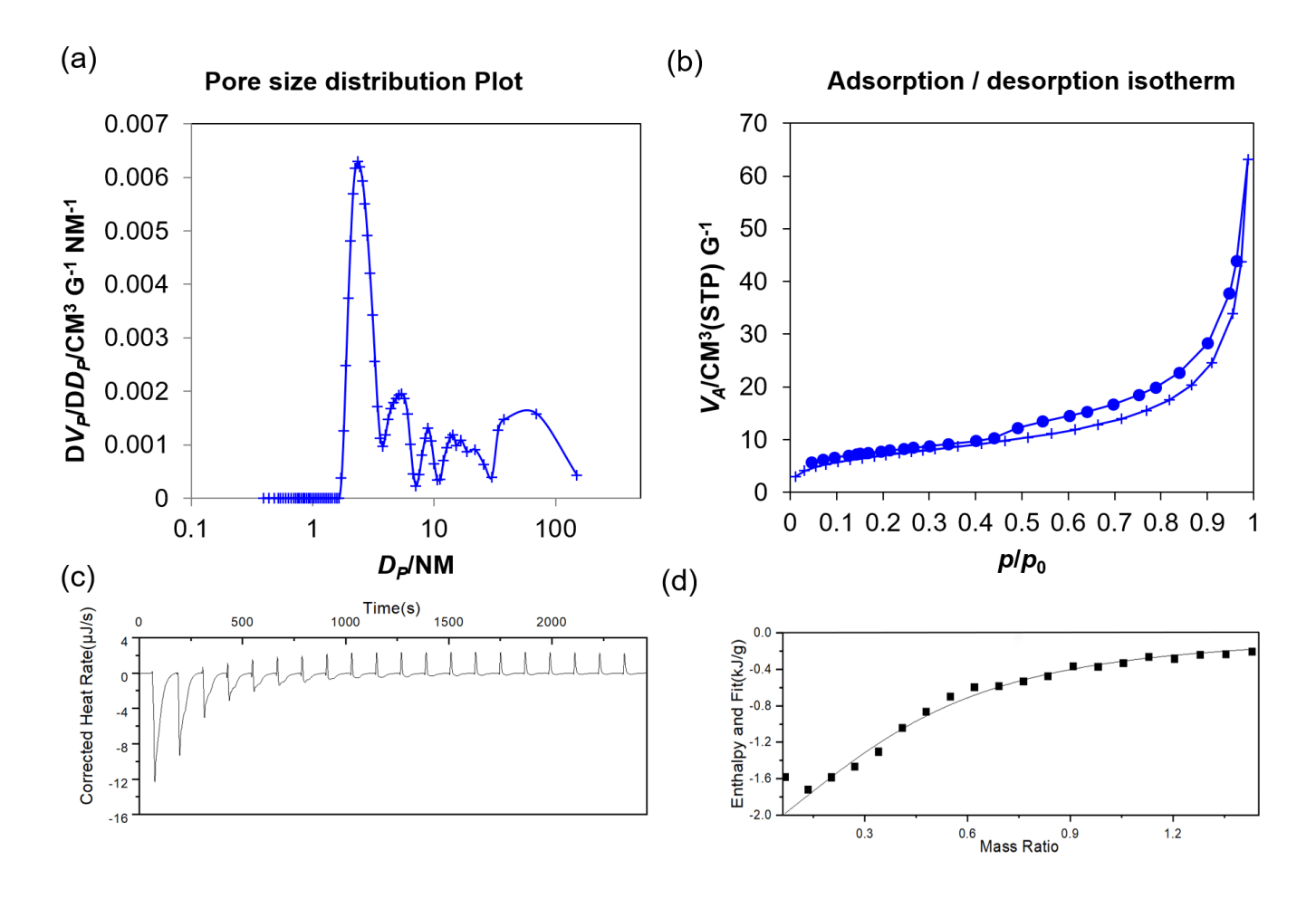


Figure S5. Brunauer-Emmett-Teller (BET) measurements of NIP sample. Fig S5. (a) demonstrates the pore distribution plot with Fig S5. (b) showing the adsorption-desorption isotherm of the NIP. The BET analysis returned a specific surface area 128.2 m2/g measured for the NIP. The pore volume of the NIP was 0.334 cm3/g, with an BJH Desorption average pore diameter of 11.4743 nm. Isothermal Titration Calorimetry (ITC) analysis of the binding interactions between the Non-Imprinted Polymer (NIP) and L-Arginine. Raw thermogram displaying the corrected heat rate ( $\mu$ J/s) versus time (s) during successive injections of the analyte into the NIP suspension (Fig. S6.c). The exothermic peaks indicate heat released upon interaction. (Fig S6.d). The analysis yields a low enthalpy change ( $\Delta$ H = -1.61 kJ·mol-1), indicating minimal thermodynamically significant interaction and confirming low non-specific binding by the NIP.

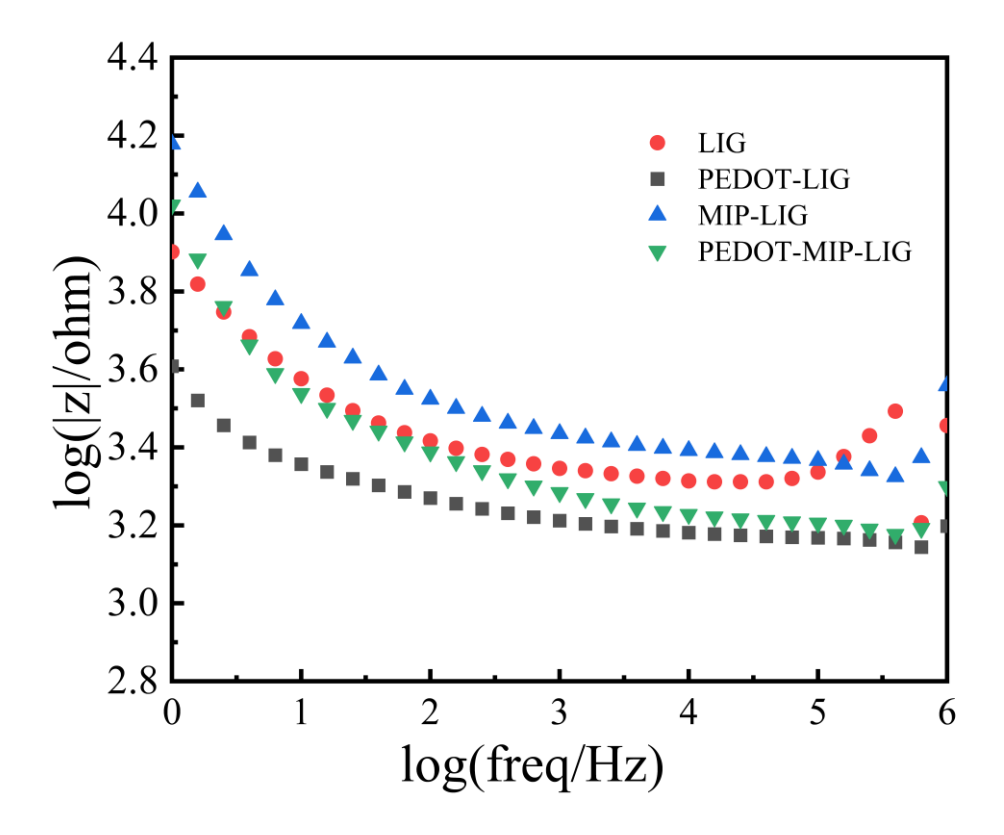


Figure S6. Evaluation of the effect of PEDOT:PSS deposition and MSM integration using Electrochemical Impedance Spectroscopy (EIS). EIS plots illustrate the impedance changes during the sequential modification of the Laser-Induced Graphene (LIG) electrode. The electrodeposition of PEDOT:PSS reduces the impedance (black squares) compared to the bare LIG electrode (red circles) across the entire frequency range (1 Hz to 1 MHz. Subsequent integration of the MIP-based MSM increases the impedance for both configurations (MIP-LIG, blue triangles, and PEDOT-MIP-LIG, green inverted triangles), a consistent increase attributed to the inherent resistance of the MSM